

# Durability and Degradation Analysis of CoFe<sub>2</sub>O<sub>4</sub> Supported on Carbon Nitride Composites for Alkaline Oxygen Evolution Reaction

Sankeerthana Bellamkonda\* and Mohamed Mamlouk

School of Engineering, Newcastle University, Newcastle upon Tyne, NE1 7RU United Kingdom

## ABSTRACT

This study investigates the oxygen evolution reaction (OER) performance and degradation mechanisms of CoFe<sub>2</sub>O<sub>4</sub> (CFO) and its composite with carbon nitride (CFO/CN). The CFO/CN electrocatalyst exhibits superior initial catalytic activity, achieving a higher current density (42 mA cm<sup>-2</sup> at 1.58 V vs. RHE), lower overpotential (359 mV at 10 mA cm<sup>-2</sup>), and a smaller Tafel slope (45.2 mV/dec) due to enhanced charge transfer, oxygen vacancy stabilization, and pseudocapacitive contributions from CN. However, prolonged cycling leads to structural degradation, oxygen vacancy depletion, and surface amorphization, resulting in performance decline. Despite this, CFO/CN maintains better stability at 10 mA cm<sup>-2</sup>, sustaining a lower operating voltage than CFO over 24 hours. Post-OER XRD and XPS confirm that CN mitigates severe catalyst degradation, preserving active sites and conductivity. These findings show that while higher activity can be achieved, maintaining long-term stability remains a challenge, highlighting the importance of developing strategies to preserve oxygen vacancies and strengthen the catalyst's structure for sustained OER performance.

**Keywords:** Cobalt ferrite, Carbon nitride, alkaline electrolysis, oxygen evolution, degradation mechanism

## 1. INTRODUCTION

The urgent global shift toward clean and sustainable energy has driven intense interest in water electrolysis for green hydrogen production, a critical energy carrier for the future.<sup>1,2</sup> Among the two half-reactions in water splitting, the oxygen evolution reaction (OER) remains a major bottleneck due to sluggish kinetics and high overpotential requirements.<sup>3-5</sup> Many OER electrocatalysts, despite exhibiting high initial activity, fail to meet durability requirements due to structural degradation, surface reconstruction, and loss of active sites during prolonged operation. One of the primary challenges is the instability of active metal species, which

---

\*Corresponding author; Tel.: +91 9445435743; +44 7471042866;

E-mail address: [sankeerthana999@gmail.com](mailto:sankeerthana999@gmail.com) (Sankeerthana B.)

undergo oxidation, dissolution, or phase transformation under harsh OER conditions, leading to reduced catalytic efficiency over time. Additionally, the formation and subsequent loss of oxygen vacancies, which are crucial for intermediate adsorption and charge transfer, further contribute to performance decline. In carbon-supported catalysts, oxidative degradation of the support at high anodic potentials often accelerates catalyst deactivation.<sup>6,7</sup> Moreover, insufficient electronic conductivity, irreversible surface passivation due to the accumulation of inactive metal oxides or hydroxides, and catalyst detachment from the electrode surface further exacerbate long-term instability.<sup>8</sup> These limitations underscore the urgent need for rational catalyst design that incorporates defect engineering, structural stabilization, and interfacial charge transfer optimization to enhance both activity and durability in practical OER applications.

Among the metal oxides, the spinel oxides, such as  $\text{CoFe}_2\text{O}_4$ , offer excellent durability in oxygen evolution reaction (OER) applications due to their robust crystalline structure, mixed valency, and strong metal-oxygen bonds. Their well-defined cubic framework provides inherent structural stability, preventing significant lattice distortion or dissolution under harsh alkaline conditions. Additionally, the presence of both tetrahedral and octahedral metal cations enables efficient redox cycling, ensuring sustained catalytic activity over prolonged operation.<sup>9-12</sup> However, despite their stability, spinel oxides often suffer from moderate electrical conductivity and limited oxygen vacancy density, which hinder charge transfer and intermediate adsorption, reducing overall catalytic efficiency. To overcome these limitations, the integration of graphitic carbon nitride (CN) offers significant advantages.<sup>13,14</sup> CN not only enhances electronic conductivity but also introduces nitrogen-rich active sites that promote oxygen intermediate adsorption. Its layered structure facilitates better dispersion of spinel oxide nanoparticles, increasing active site accessibility and preventing aggregation.<sup>15,16</sup> Moreover, CN contributes to the formation and stabilization of oxygen vacancies, further optimizing the reaction kinetics. By combining the structural durability of spinel oxides with the electronic and defect-engineering benefits of CN, the resulting composite catalyst achieves improved long-term stability and enhanced OER performance.

In this study, we systematically investigated the structural, electronic, and electrocatalytic properties of CFO and its composite with graphitic carbon nitride (CFO/CN) as OER catalysts in alkaline media. The integration of CN was designed to enhance the catalytic performance of CFO by improving conductivity, increasing oxygen defect density, and stabilizing active sites. Besides comprehensive electrochemical characterization, the Distribution of Relaxation Times

(DRT) analysis provided deeper mechanistic insights into the electrochemical processes influencing catalyst performance and degradation. Post-OER structural and surface analyses, including XRD and XPS, further examined lattice distortions, oxygen vacancy changes, and surface transformations. This work provides valuable design principles for optimizing spinel oxide-based OER catalysts and highlights the importance of stabilizing oxygen defects and active sites for durable alkaline water electrolysis.

## **2. EXPERIMENTAL SECTION**

### **2.1 Materials**

Unless otherwise specified, all the chemicals employed in this study were used as received without any further purification.  $\text{Fe}(\text{NO}_3)_3 \cdot 9\text{H}_2\text{O}$  (99.9%, SD Fine),  $\text{Co}(\text{NO}_3)_2 \cdot 6\text{H}_2\text{O}$  (99.9%, SD Fine), sodium acetate (Thomas-Baker), melamine (Merck). Deionized (DI) water was used in all the experiments.

### **2.2 Synthesis of CFO/CN nanocomposites**

Iron nitrate ( $\text{Fe}(\text{NO}_3)_3 \cdot 9\text{H}_2\text{O}$ ), cobalt nitrate ( $\text{Co}(\text{NO}_3)_2 \cdot 6\text{H}_2\text{O}$ ), sodium acetate, melamine, and ethanol were used as such without any further purification. Firstly, 0.1 M  $\text{Fe}(\text{NO}_3)_3 \cdot 9\text{H}_2\text{O}$ , 0.05 M  $\text{Co}(\text{NO}_3)_2 \cdot 6\text{H}_2\text{O}$ , and 0.05 M of protonated CN were individually dissolved in 20 mL ethanol each and stirred for 1 h. After 1 h, sodium acetate was added into the mixture and magnetically stirred for 2 h. The mixture was then transferred into a 100 mL Teflon lined stainless steel autoclave and heated at 200 °C for 18 h. The autoclave was then allowed to cool to room temperature. The obtained brown precipitates were centrifuged 6-7 times to remove the residues. The centrifuged product was then dried at 80 °C overnight and was calcined at 350 °C for 3h to obtain CFO/CN nanocomposite. The CFO was also synthesized using the same procedure with their respective precursors. Protonated graphitic carbon nitride synthesized earlier in our lab was used as such. In brief, 1.5 mL of 37% conc. HCl was added to hot melamine solution under stirring. The solution was then transferred to an oven at 120 °C to evaporate the water. The resulting solid was placed in a covered crucible and heated at 500°C in a muffle furnace for 2 h with heating rate 20 °C/ min and further heated at 520 °C for 2 h.

### **2.3 Materials characterization**

The structural analyses of the composites were done by powder X-ray diffraction (PXRD), Fourier transform infrared (FT-IR) and Raman measurements. Bruker AXS D8 advanced diffractometer was used to obtain PXRD profiles employing  $\text{Cu K}\alpha$  ( $\lambda = 0.15406$  nm) radiation.

The KBr pellet method was used to record FT-IR spectra by JASCO FT-IR-4100 spectrophotometer. The Raman measurements were obtained at room temperature by BRUKER RFS 27 with a 627 nm laser as source. Surface morphologies of the photocatalysts were characterized by field emission scanning electron microscopy (FESEM) and high-resolution transmission electron microscopy (HRTEM) images employing JEOL JEM 3010 with an accelerating voltage of 200 kV. The X-ray photoelectron spectroscopy (XPS) spectra were recorded using ESCA+ (Omicron nanotechnology, Oxford Instrument, Germany) equipped with monochromatic aluminum source (Al K $\alpha$  radiation  $h\nu$  = 1486.6 eV), operated at 15 kV and 20 mA. The C 1s binding energy 284.6 eV is taken as a reference.

## 2.4 Electrochemical measurements

The electrochemical measurements were performed using an Autolab potentiostat/galvanostat (Metrohm Autolab PGSTAT302N). The standard hydrogen electrode (SHE) and graphite rod were used as the reference and counter electrodes, respectively. The working electrodes were fabricated as follows: a total of 10 mg of the catalyst powder was well dispersed in a mixture of polyvinylidene fluoride (PVDF) in an N-methyl-2-pyrrolidone (NMP) solution (200  $\mu$ L) in weight ratio of 5:1 to achieve a homogeneous catalyst ink. The resulting catalyst ink was dropped onto the surface of a Au mesh (1 cm<sup>2</sup> area) by using micropipette tip and left to dry at room temperature. The catalyst loading on each of the Au mesh is 0.24 mg cm<sup>-2</sup>. Linear sweep voltammetry (LSV), cyclic voltammetry (CV) and chronoamperometry (CA) measurements were carried out in 1 M KOH solution at room temperature. Overpotential ( $\eta$ ) was computed based on the equation:  $\eta$  (V) = E (RHE) – 1.23 V. The Tafel plots were obtained from the LSV polarization curves by using the Tafel relation as  $\eta = a + b \log j$ , where  $j$  and  $b$  indicates the current density and Tafel slope. Electrochemical impedance spectroscopy (EIS) of the electrodes were evaluated by a PARSTAT 2273 potentiostat at an open-circuit voltage (OCV) in the frequency range of 100 kHz to 0.01 Hz with the AC voltage amplitude of 10 mV. DRT analysis was used to assist the deconvolution of the obtained EIS data using DRT tools software.<sup>17</sup>

### 3. RESULTS AND DISCUSSION

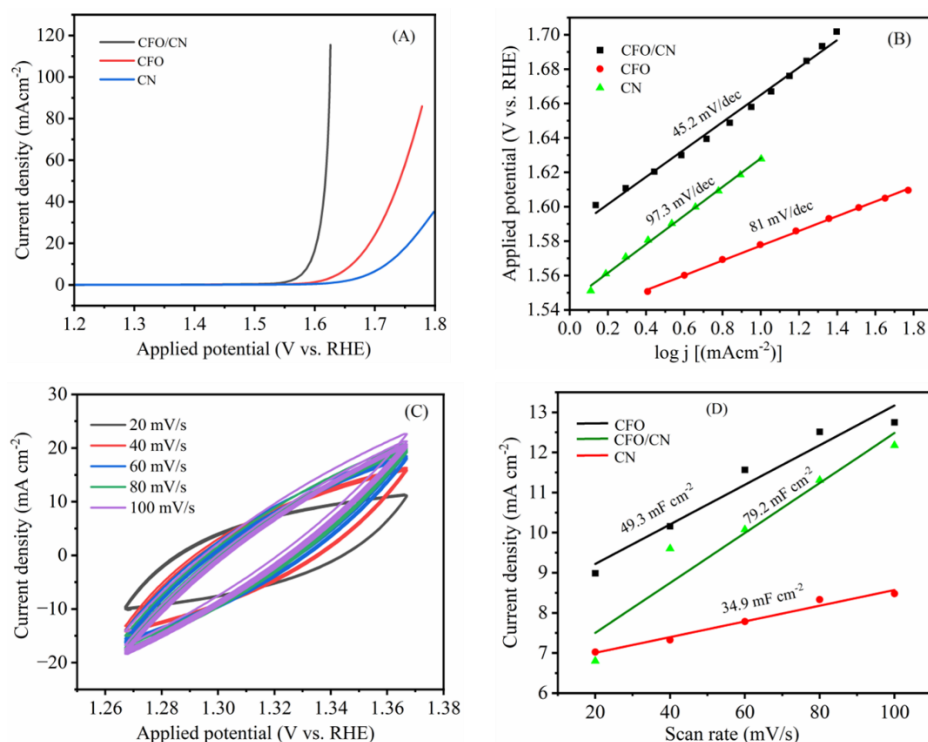


**Figure 1.** (A) LSV plots obtained with CFO/CN, CFO, and CN for OER at 5  $\text{mV s}^{-1}$  in 1.0M KOH, (B) Tafel slopes obtained with CFO/CN, CFO, and CN, (C) Electrochemical active surface area (ECSA) of CFO/CN, and (D) Electrochemical double-layer capacity ( $C_{dl}$ ) of CFO/CN, CFO and CN.

Electrocatalytic activity of CFO and CFO/CN samples is evaluated in both their pristine states and after various CV cycles, under OER conditions in 1.0 M KOH. The LSV curves of all the samples were recorded at 5  $\text{mV s}^{-1}$ , as shown in Figure 1A. The current density values were normalized to the geometric surface area of the Au mesh electrodes. Figure 1A demonstrates that CFO/CN exhibits superior OER performance compared to pristine CFO and CN. This is evident from the lower overpotential of CFO/CN (359 mV at a current density of 10  $\text{mA cm}^{-2}$ ) compared to CFO (432 mV at 10  $\text{mA cm}^{-2}$ ). Additionally, the CFO/CN composite achieves a Tafel slope of 45.2 mV/dec (Figure 1B), significantly lower than the Tafel slope of CFO, which is 81 mV/dec (Figure 1B). These results indicate faster charge transfer kinetics for OER on the CFO/CN composite compared to CFO. Moreover, the Tafel slope of CFO/CN is also lower than that reported for many pristine  $\text{Co}_3\text{O}_4$  and Co-based spinel oxides<sup>18</sup>, which typically exhibit Tafel slopes around 60 mV/dec. The OER activity of the electrocatalysts was further evaluated by measuring the ECSA, which investigates the exposure of the active sites. ECSA is directly related to the electrochemical double-layer capacitance ( $C_{dl}$ ) and computed from the

non-Faradaic region of the CV curves. The capacitive behavior, assessed via cyclic voltammetry at varying scan rates (Figure 1C), reveals a higher  $C_{dl}$  for CFO/CN ( $79.2 \text{ mF cm}^{-2}$ ) compared to CFO ( $49.3 \text{ mF cm}^{-2}$ ) and CN ( $34.9 \text{ mF cm}^{-2}$ ), as shown in Figure 1D. This higher  $C_{dl}$  for CFO/CN reflects a larger electrochemically active surface area, attributed to the effective integration of CN, which increases active site accessibility and stabilizes oxygen vacancies. These results collectively establish CFO/CN as the most efficient catalyst among the three, benefiting from the combined advantages of redox activity (CFO) and conductivity and structural support of CN.

The cyclic voltammetry (CV) profiles in Figures 2A and 2B illustrate the OER performance of CFO/CN and CFO over 0, 100, 500, and 1000 cycles. As shown in Figure 2A, the CFO/CN composite exhibits superior catalytic activity at the 100th cycle, achieving a higher current density of  $42 \text{ mA cm}^{-2}$  and a lower overpotential at  $10 \text{ mA cm}^{-2}$  compared to CFO (Figure 2B). This improved performance can be attributed to the synergistic interaction between CFO and CN, which enhances charge transfer efficiency, stabilizes oxygen vacancies, and introduces pseudocapacitive behavior. However, both CFO/CN and CFO display a gradual decline in catalytic activity with increasing CV cycles (100, 500, 1000), as shown in Figures 2C and D. From Figure 2E, the Tafel slope for CFO/CN increases to  $77.8 \text{ mV dec}^{-1}$  after 1000 cycles, nearly double its pristine value ( $45.2 \text{ mV/dec}$ ), while the Tafel slope of CFO reaches a comparable  $87.6 \text{ mV dec}^{-1}$ , representing a smaller relative increase from  $79.3 \text{ mV/dec}$ . Despite its initial superior OER activity, CFO/CN experiences significant performance degradation with cycling, eventually approaching the activity level of CFO. The decline in CFO/CN could be associated with the loss of active sites, reduced pseudocapacitive contributions, and structural transformations, including the formation of less active phases such as  $(\text{Co, Fe})\text{OOH}$  and  $(\text{Co, Fe})\text{O}_2$ .

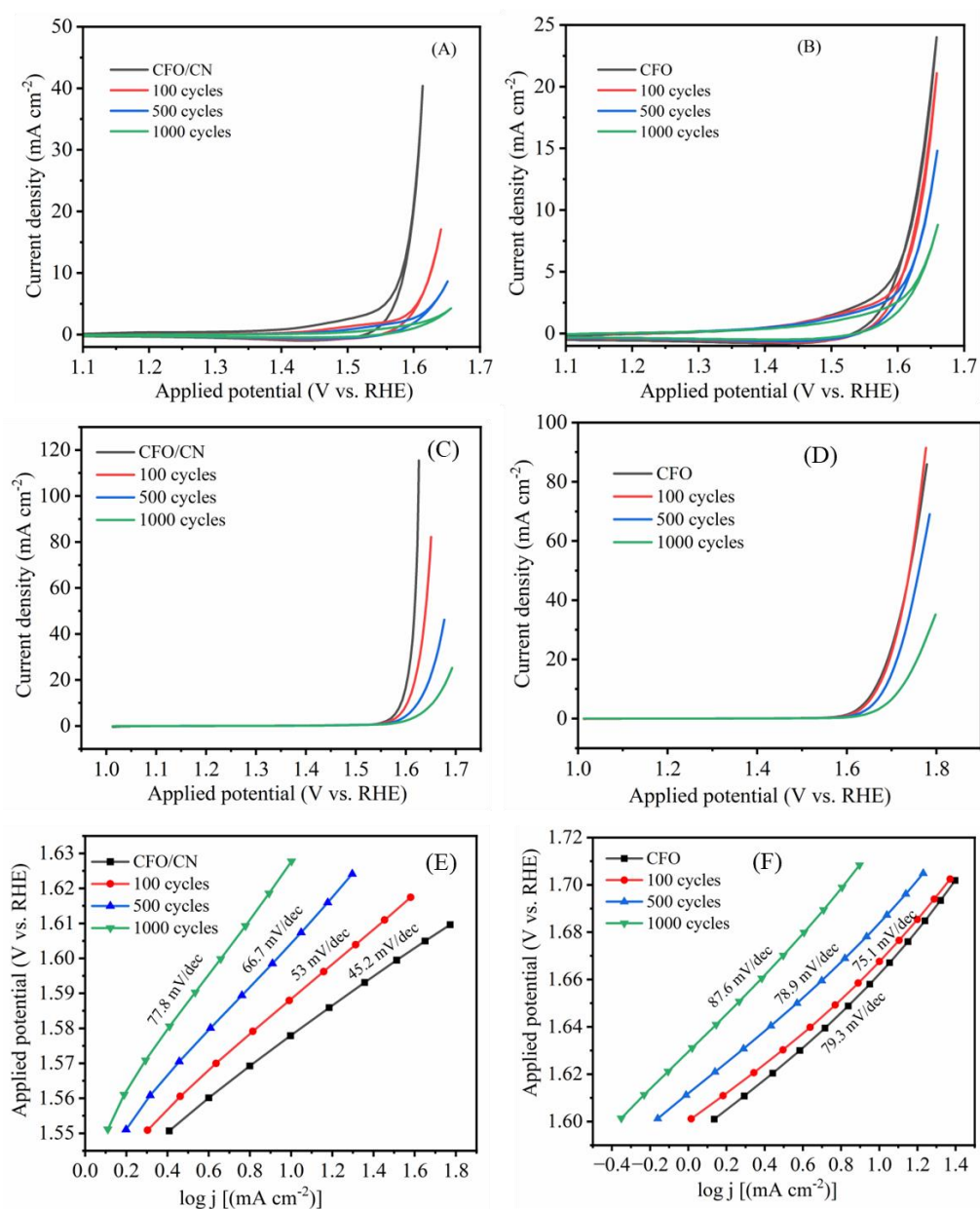


**Figure 2.** (A, B) CVs (C,D) LSVs and (E,F) Tafel slopes of CFO/CN and CFO run for 0, 100, 500 and 1000 cycles at 5 mVs<sup>-1</sup> in 1 M KOH solution (without stirring).



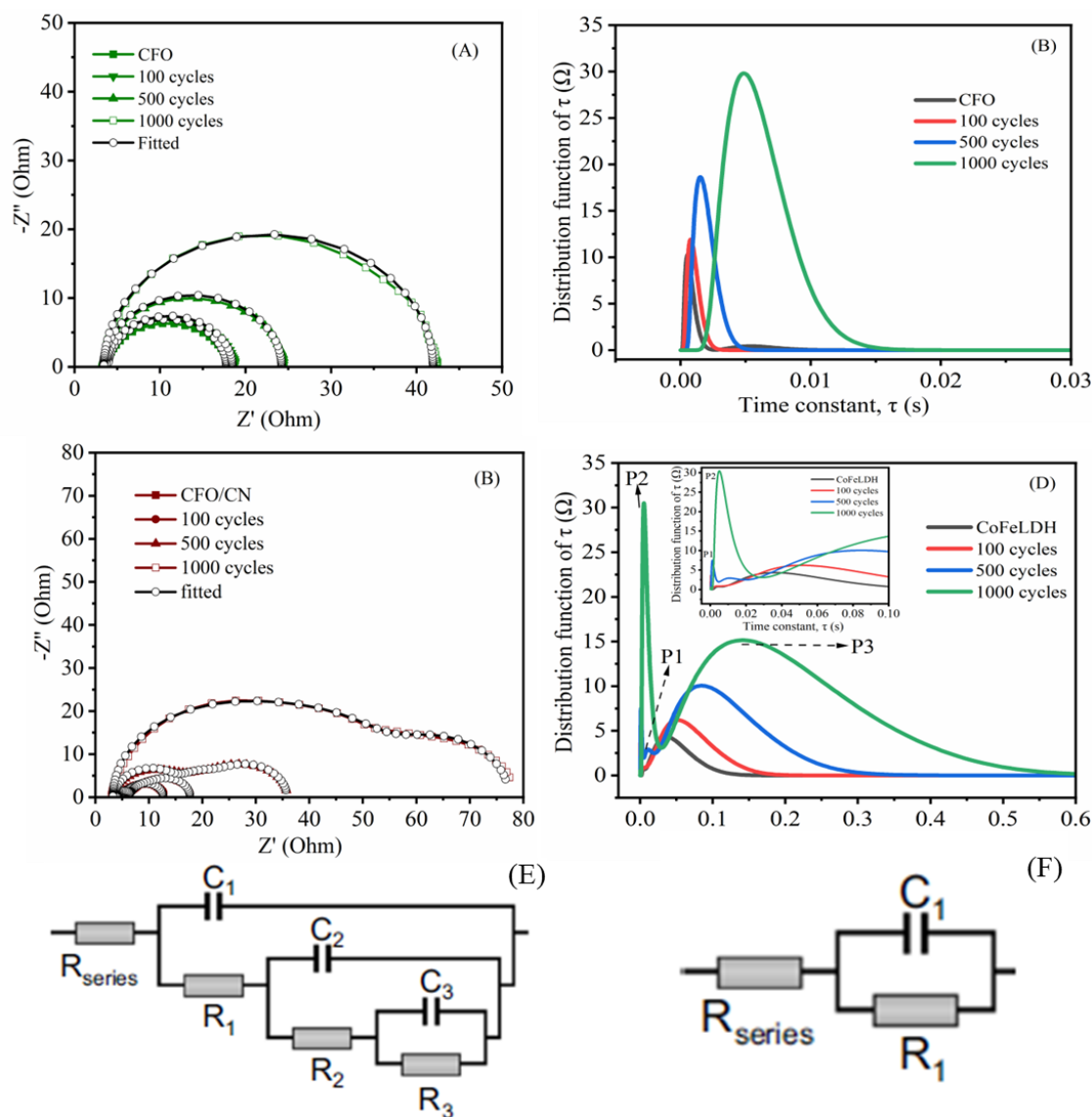


**Figure 3.** (A, C) Nyquist plots of respective CFO and CFO/CN; (B, D) distribution of relaxation time (DRT) analysis of respective CFO and CFO/CN electrodes done after 100, 500 and 1000 cycles of CV; (E, F) Respective corresponding equivalent circuits of CFO/CN and CFO.

To better understand the deactivation mechanisms of spinel oxide nanoparticles during the OER, EIS was employed to probe the underlying electrochemical processes. The Nyquist and distribution of relaxation time (DRT) plots for CFO and CFO/CN provide detailed insights into their electrochemical behavior during the oxygen evolution reaction (OER), highlighting the differences in charge transfer, pseudocapacitive properties, and degradation mechanisms over cycling. The Nyquist plots for CFO (Figure 3A) show a single semicircle across all cycles, corresponding to the charge transfer resistance  $R_{ct}$  at the electrode/electrolyte interface. In its pristine state, the small semicircle diameter indicates relatively moderate charge transfer



resistance. However, with increasing cycling (100, 500, 1000 cycles), the semicircle grows significantly, reflecting an increase in  $R_{ct}$ . All the resistance and capacitance values obtained from the EIS fitting are presented in Table 1. This behavior aligns with a degradation in the catalytic performance, attributed to structural changes such as the formation of less conductive (Co,Fe)OOH or (Co,Fe)O<sub>2</sub> phases, which hinder efficient electron transfer. The corresponding DRT analysis (Figure 3B) reveals a single peak (P1) at low time constants, representing charge transfer processes. Over cycling, the peak broadens and shifts to higher time constants, signifying slower charge transfer kinetics due to surface passivation and a loss of active sites.

**Table 1.** Resistance and capacitance values obtained for electrochemical circuit modeling of Nyquist plots of CFO and CFO/CN taken after 0, 100, 500, 1000 CV cycles

Number of cycles	Resistance				Capacitance/F		
CFO/CN	$R_{series}$	R1	R2	R3	C1	C2	C3
0	3.78988	1.29121	3.71558	3.88092	7.99E-05	0.00209	0.0069
100	3.84271	2.9454	6.10132	4.80696	7.40E-05	0.00215	0.00949
500	3.62872	13.38859	9.63392	9.14092	8.17E-05	0.00156	0.0084
1000	3.27077	42.05983	15.09691	16.88846	9.72E-05	8.82E-04	0.00693
CFO							
0	3.93306	13.83283	-	-	3.87E-05	-	-
100	3.66681	14.78946	-	-	5.05E-05	-	-
500	3.37209	20.83958	-	-	7.12E-05	-	-
1000	3.44422	38.49482	-	-	1.00E-04	-	-

In contrast, the Nyquist plots for CFO/CN (Figure 3C) exhibit two distinct semicircles, indicating the presence of multiple electrochemical processes. The high-frequency semicircle corresponds to charge transfer at the electrode interface  $R_{ct}$ , while the low-frequency semicircle reflects pseudocapacitive behavior associated with reversible redox transitions and adsorption/desorption of oxygen intermediates (e.g., OH<sup>-</sup>, OOH<sup>-</sup>) facilitated by the synergy between CFO and CN. Over cycles, both semicircles grow in diameter, suggesting an increase in resistance due to structural degradation and reduced oxygen vacancy density.

The DRT plots for CFO/CN (Figure 3D) provide deeper insights into these processes, with three peaks (P1, P2, P3) identified:

DRT peak (P)	Analysis
P1	Appearing at low time constants, corresponds to the charge transfer process at the electrode/electrolyte interface. The intensity decreases, and the time constant increases over cycling, indicating a loss in charge transfer efficiency due to passivation and reduced conductivity. <sup>19</sup>
P2	The intermediate peak represents pseudocapacitive processes, such as the reversible redox transitions of $\text{Co}^{2+}/\text{Co}^{3+}$ and $\text{Fe}^{2+}/\text{Fe}^{3+}$ ions. This peak diminishes significantly with cycling, reflecting a loss of pseudocapacitive contributions as active sites are deactivated and oxygen vacancies are filled.
P3	The high time constant peak is associated with slower diffusion-controlled processes, such as the movement of hydroxyl ions ( $\text{OH}^-$ ) within the interlayer regions or at the electrode surface. The broadening and shift of P3 to higher time constants suggest increased diffusion resistance due to structural collapse and blocked pathways.

From these observations, it says that CFO predominantly relies on a single charge transfer mechanism, CFO/CN initially benefits from the combined contributions of charge transfer and pseudocapacitive processes, leading to superior catalytic performance. However, the advantages provided by the synergistic interaction in CFO/CN become a limitation during extended cycling, resulting in significant performance degradation. This underscores the critical importance of stabilizing the composite structure and preserving oxygen vacancy density in CFO/CN to maintain sustained catalytic activity and efficiency under prolonged OER conditions.

To understand the structural transformations or modifications leading to OER deactivation, XRD and XPS analyses were conducted. Figures 4(A) and 4(B) present the O 1s spectra for pristine CFO and post-OER CFO/CN. Before OER, the peaks for CFO/CN at 530.24 eV are associated with metal-bound oxygen ( $\text{O}_\text{I}$ ), and ~531.29 eV (CFO/CN) ( $\text{O}_\text{II}$ ) correspond to oxygen defects or vacancies.<sup>20,21</sup> The pristine CFO/CN catalyst exhibits a high intensity of  $\text{O}_\text{II}$ , indicating a significant presence of oxygen vacancies that enhance charge transfer and intermediate adsorption, thereby promoting catalytic activity. However, after OER, the  $\text{O}_\text{II}$  peak shifted to 531.3 eV with a noticeable decrease in intensity suggesting the partial loss or filling of oxygen vacancies during prolonged electrochemical operation, contributing to catalyst degradation. Additionally, an increase in  $\text{O}_\text{III}$  and  $\text{O}_\text{IV}$  after OER indicates enhanced surface adsorption of hydroxyl groups and water molecules, which may be linked to the formation of passivating layers such as (Co, Fe)OOH.<sup>22</sup>

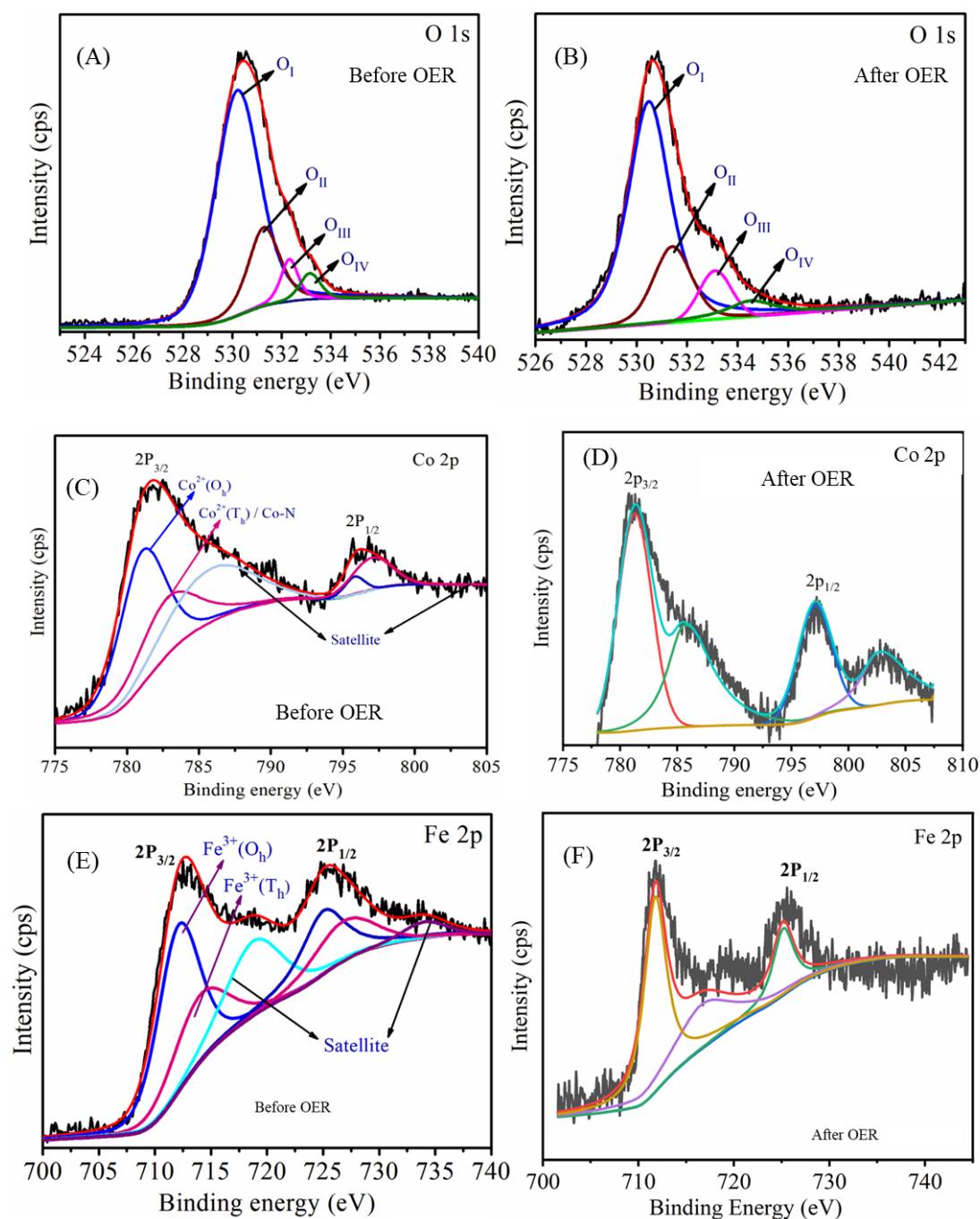


**Figure 4.** (A, B) O 1s; (C, D) Co 2p; and (E, F) Fe 2p XPS spectra of CFO/CN electrocatalysts before and after OER.

From Figures 4(C) and 4(D), before OER, Co  $2p_{3/2}$  exhibits distinct peaks corresponding to  $\text{Co}^{2+}$  in tetrahedral ( $T_h$ ) and octahedral ( $O_h$ ) coordination, along with Co-N interactions, indicating strong metal-support interactions between CFO and CN.<sup>23</sup> Satellite peaks further confirm the presence of  $\text{Co}^{2+}$  species, which contribute to catalytic activity by facilitating

charge transfer and intermediate adsorption. After OER, the Co 2p<sub>3/2</sub> peak shifts toward higher binding energies, accompanied by a reduction in Co<sup>2+</sup> intensity and the emergence of Co<sup>3+</sup> species, suggesting oxidation of Co<sup>2+</sup> to Co<sup>3+</sup> and potential Co<sup>4+</sup> formation. This transformation indicates the active role of Co in redox transitions during OER, enhancing catalytic efficiency. However, the decrease in satellite peak intensity post-OER suggests there could be possible deactivation of some active Co sites. These findings confirm that the oxidation state evolution of Co in CFO/CN plays a crucial role in its OER performance.

From Figures 4(E) and 4(F), for pre-OER CFO/CN, Fe 2p<sub>3/2</sub> exhibits peaks corresponding to Fe<sup>3+</sup> in tetrahedral (T<sub>h</sub>) and octahedral (O<sub>h</sub>) coordination, confirming the presence of a stable spinel structure.<sup>20,21</sup> The prominent satellite peaks further validate the high-spin Fe<sup>3+</sup> state, which plays a crucial role in facilitating electron transfer during OER. However, after OER, the post-electrolysis spectrum shows significant changes, including peak broadening and shifts toward higher binding energies, indicating oxidation of Fe<sup>3+</sup> and potential Fe<sup>4+</sup> formation. The reduction in satellite peak intensity post-OER suggests partial deactivation of Fe sites, likely due to structural rearrangements and surface passivation by (Co,Fe)OOH-like phases.<sup>22</sup> These changes correlate with the observed degradation in OER performance, as the loss of redox-active Fe species and the formation of insulating surface layers reduce the efficiency of electrocatalyst.

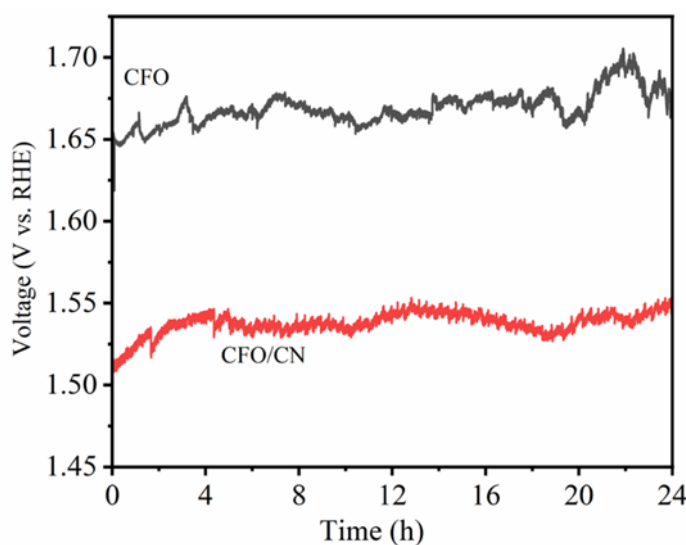


**Figure 5.** Chronopotentiometry durability test of CFO/CN and CFO at a constant current density of 10 mA cm<sup>-2</sup>.

Despite the observed degradation of CFO/CN through EIS, CV, LSV, and DRT analyses, corroborated by XPS, the catalyst maintains superior stability at  $10 \text{ mA cm}^{-2}$  compared to CFO, highlighting its durability under practical OER conditions. This stability can be attributed to several key factors. First, CFO/CN operates at a significantly lower overpotential than CFO, and while some increase in charge transfer resistance ( $R_{ct}$ ) occurs over prolonged cycling, the improved electronic conductivity and interfacial charge transport facilitated by CN mitigate severe performance losses. Second, although XPS confirms a reduction in oxygen vacancies post-OER, the remaining vacancies in CFO/CN continue to enhance reaction kinetics, whereas CFO, which inherently has fewer oxygen defects, experiences more pronounced activity loss. The presence of CN also helps stabilize oxygen vacancies, slowing their complete depletion and maintaining catalytic efficiency over time. Third, while DRT analysis indicates a decline in pseudocapacitive behavior, the residual charge storage capability of CN still contributes to efficient intermediate adsorption and desorption, keeping the OER process active despite partial deactivation of active sites. Furthermore, CN prevents excessive agglomeration of CFO nanoparticles, ensuring better dispersion and sustained exposure of active sites, whereas CFO alone is more prone to particle aggregation and passivation. Additionally, the layered structure of CN resists complete surface oxidation, unlike CFO, which is more susceptible to irreversible transformation into less conductive (Co,Fe)OOH phases. These combined effects result in the CFO/CN composite demonstrating a more stable voltage profile over 24 hours, with minimal fluctuations at  $10 \text{ mA cm}^{-2}$ , while CFO exhibits greater instability and a gradual increase in operating voltage. Thus, although CFO/CN undergoes degradation over extended cycling, its enhanced oxygen vacancy retention, charge transfer capability, pseudocapacitive contributions, and structural stability allow it to maintain superior long-term durability at practical current densities, making it a more effective catalyst for alkaline water electrolysis.

To further elucidate the role of CN in stabilizing active sites in CFO/CN electrocatalyst and maintaining its durability, the XPS spectra of C 1s and N 1s before and after OER of CFO/CN are investigated, as shown in Figure 6. In the C 1s spectra (Figures 6(A) and 6(B)), the dominant peak corresponding to N–C=N ( $\sim 288.0 \text{ eV}$ ), characteristic of the heptazine structure in CN, remains largely unchanged after OER, confirming the structural integrity of CN. The C–C/C=C peak ( $\sim 284.6 \text{ eV}$ ) also remains stable, indicating that CN does not undergo significant oxidative degradation, which is a common issue in conventional carbon supports. In the N 1s spectra (Figures 6(C) and 6(D)), the presence of N–C=N ( $\sim 398.2$  to  $398.85 \text{ eV}$ ) before and after OER suggests that the catalytic nitrogen sites remain intact, further supporting the durability of CN

under OER conditions. Notably, a shift and slight increase in the Co-N peak ( $\sim 397.8$  eV) after OER indicate stronger electronic interactions between CFO and CN, which may contribute to improved charge transfer and active site stabilization. The emergence of an intensified C-NH/N-(C)<sub>3</sub> peak ( $\sim 400.5$  eV) post-OER suggests increased adsorption of hydroxyl species or interaction with oxygen intermediates, highlighting the role of CN in facilitating oxygen vacancy retention and catalytic activity.<sup>24,25</sup> These findings align with the electrochemical stability results, reinforcing that CN not only enhances initial catalytic performance but also plays a critical role in maintaining structural integrity, preventing excessive oxidation, and preserving active sites, ultimately contributing to the superior long-term durability of CFO/CN compared to CFO.

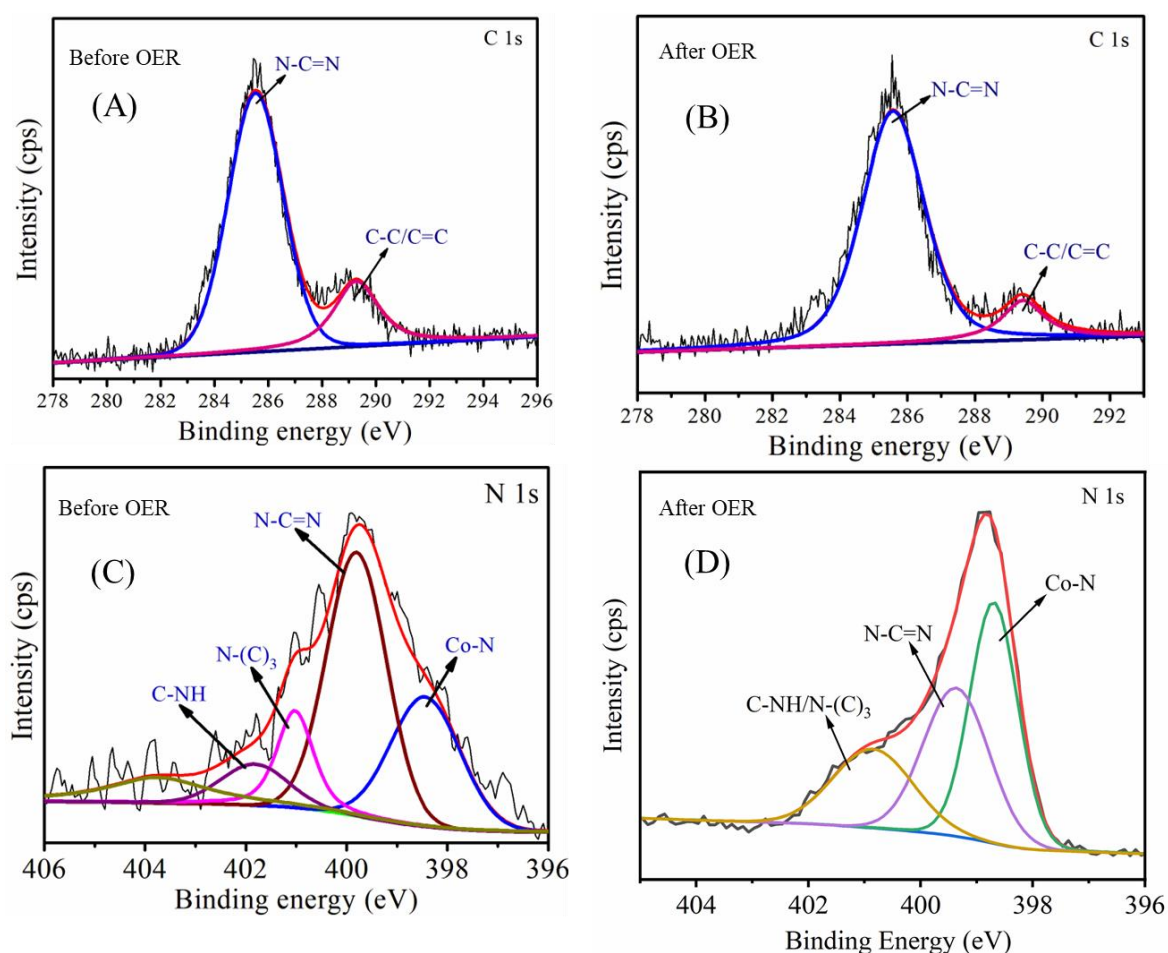


**Figure 6.** (A, B) C 1s and (C, D) N 1s spectra of CFO/CN electrocatalysts before and after OER.

To further investigate lattice distortions and structural transformations of CFO/CN after OER, the XRD patterns of CFO, CFO/CN, and post-OER CFO/CN were analysed, as shown in Figure 7. The CFO diffraction peaks observed at  $2\theta = 30.1^\circ$ ,  $35.4^\circ$ ,  $43.1^\circ$ ,  $57.0^\circ$ , and  $62.6^\circ$  are well



indexed to the (220), (311), (400), (511), and (440) planes of the cubic spinel structure of cobalt ferrite (JCPDS No. 22-1086)<sup>26</sup>, confirming its crystalline nature. In the CFO/CN composite, an additional peak at approximately 27.2° corresponds to the (002) plane of carbon nitride, indicating the successful integration of CN into the composite structure. However, after OER, the XRD of CFO/CN exhibits lowered peak intensities and increased amorphization, indicating partial structural degradation while retaining some degree of crystallinity. Compared to the pre-OER pattern, the weakened diffraction peaks suggest that prolonged electrochemical cycling induces surface restructuring, disordering, and possible phase transformations, but does not destroy the spinel framework completely. The persistence of some peaks, albeit with reduced intensity, implies that a fraction of the crystalline CFO structure remains intact, while the loss of intensity points to the formation of an amorphous (Co,Fe) oxyhydroxide (OOH) layer on the surface, which is a common phenomenon in transition metal-based OER catalysts. This observation aligns well with XPS results, which show changes in oxidation states and oxygen vacancy evolution, as well as EIS data, which indicate increased charge transfer resistance after OER. Despite these structural modifications, the CFO/CN composite continues to demonstrate relatively stable electrochemical performance, as evidenced by chronopotentiometry at 10 mA cm<sup>-2</sup>, suggesting that the residual crystalline structure, combined with the amorphous active layer, contributes to sustaining catalytic activity over extended operation.

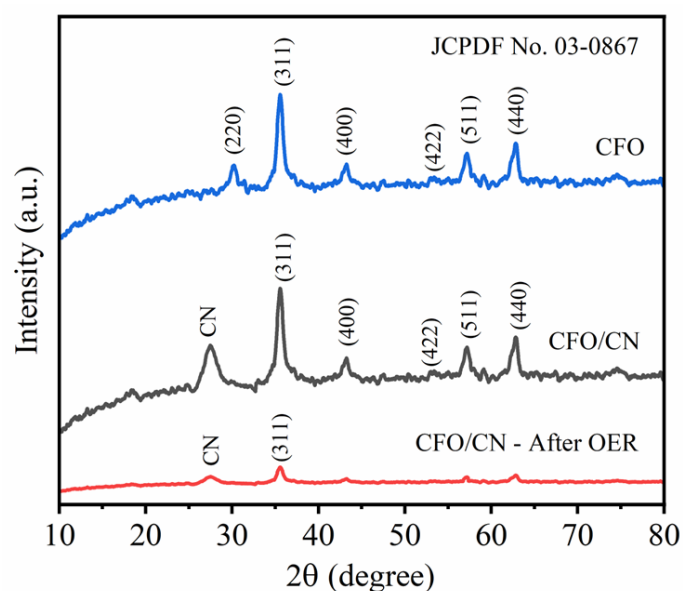


**Figure 7.** PXRD profiles of CFO, pristine CFO/CN and post-OER CFO/CN electrocatalysts.



#### 4. CONCLUSION

In conclusion, this study provides a comprehensive evaluation of the catalytic performance and durability of CFO and its composite with CN (CFO/CN) for the OER. CFO/CN exhibits superior initial activity, with lower overpotential and enhanced charge transfer kinetics, attributed to the synergistic effect of CFO and CN, which improves electron transport, stabilizes oxygen vacancies, and facilitates pseudocapacitive behavior. Despite the observed electrochemical degradation in EIS, CV, LSV, and DRT analyses, CFO/CN maintains better long-term stability at  $10 \text{ mA cm}^{-2}$  compared to CFO, as confirmed by chronopotentiometry, where it operates at a consistently lower voltage over 24 hours. The post-OER XPS and XRD analyses reveal that CFO/CN undergoes surface amorphization and oxygen vacancy depletion, but the retention of active nitrogen species in CN helps sustain catalytic performance. In contrast, CFO alone shows a greater increase in charge transfer resistance and structural degradation, leading to a more pronounced decline in OER activity over time. These findings demonstrate that while CFO/CN experiences some degradation, it outperforms CFO in both catalytic efficiency and operational durability. This work underscores the importance of oxygen vacancy stabilization, structural integrity, and interfacial charge transfer enhancements in designing durable and high-performance OER catalysts.

#### Declaration of competing interest

The authors declare that they have no known competing financial interests or personal relationships that could have appeared to influence the work reported in this paper.

#### ACKNOWLEDGEMENTS

SB thanks Dr. Souvik Roy from the School of Chemistry, University of Lincoln, UK, for providing access to his lab for the use of the autoclave and hydrothermal reactor for sample synthesis. We also thank the Department of Materials, Imperial College London, for the XPS data, as well as the School of Engineering, Newcastle University, for their support and resources.

## REFERENCES

- (1) Chu, S.; Cui, Y.; Liu, N. The path towards sustainable energy. *Nat. Mater.* **2017**, *16*, 16-22.
- (2) Dou, Y.; Liao, T.; Ma, Z.; Tian, D.; Liu, Q.; Xiao, F.; Sun, Z.; Kim, J. H.; Xue Dou, S. New insights into the stability of a high-performance nanostructured catalyst for sustainable water electrolysis. *Nano Energy*. **2016**, *30*, 267-275.
- (3) Ami, T.; Oka, K.; Kasai, H.; Kimura, T. Developing porous electrocatalysts to minimize overpotential for the oxygen evolution reaction. *Dalton Trans.* **2024**, *53*, 8563-8575.
- (4) Zhao, Y.; Dongfang, N.; Huang, C.; Erni, R.; Li, J.; Zhao, H.; Pan, L.; Iannuzzi, M.; Patzke, G. R. Operando monitoring of the functional role of tetrahedral cobalt centers for the oxygen evolution reaction. *Nat Commun.* **2025**, *16*, 580.
- (5) Jones, T. E.; Teschner, D.; Piccinin, S. Toward Realistic Models of the Electrocatalytic Oxygen Evolution Reaction. *Chem. Rev.* **2024**, *124*, 9136–9223.
- (6) Ku, Yu-P.; Kumar, K.; Hutzler, A.; Götz, C. Vorochta, M.; Sougrati, M. T.; Lloret, V.; Ehelebe, K.; Mayrhofer, Karl J. J.; Thiele, S.; Khalakhan, I.; Böhm, T.; Jaouen, F.; Cherevko, S. Impact of Carbon Corrosion and Denitrogenation on the Deactivation of Fe–N–C Catalysts in Alkaline Media. *ACS Catal.* **2024**, *14*, 8576–8591.
- (7) Jia, Y.; Li, Y.; Zhang, Q.; Yasin, S.; Zheng, X.; Ma, K.; Hua, Z.; Shi, J.; Gu, C.; Dou, Y.; Dou, S. Deactivation mechanism for water splitting: Recent advances. *Carbon Energy*. **2024**, *6*, e528.
- (8) Zlatar, M.; Escalera-López, D.; Rodríguez, M. G.; Hrbek, T.; Götz, C. Mary Joy, R.; Savan, A.; Tran, Hoang P.; Nong, H. N.; Pobedinskas, P.; Briega-Martos, V.; Hutzler, A.; Böhm, T.; Haenen, K.; Ludwig, A.; Khalakhan, I.; Strasser, P.; Cherevko, S. Standardizing OER Electrocatalyst Benchmarking in Aqueous Electrolytes: Comprehensive Guidelines for Accelerated Stress Tests and Backing Electrodes. *ACS Catal.* **2023**, *13*, 15375–15392.
- (9) Xie, W.; Ong, Samuel Jun H.; Shen, Z.; Tian, L.; Tang, K.; Xi, S.; Xu, Zhichuan J. Critical Role of Tetrahedral Coordination in Determining the Polysulfide Conversion Efficiency on Spinel Oxides. *J. Am. Chem. Soc.* **2025**, *147*, 988–997.
- (10) Hengqi, L.; Rui, X.; Shengyu, M.; Ran, W.; Zhiguo, L.; Tai Y.; Bo, S. Recent advances in noble-metal-free bifunctional oxygen electrode catalysts. *Energy Adv.* **2025**, *4*, 55-83.

- (11) Mahmoud, G. A.; Ying, F. T.; Xiao, C.; Ahmed, S. R.; Yanan, F.; Mengyuan, Z.; Anqi, S.; Sing, Y. C.; Andrivo, R.; Lydia, H. W. Cation Migration-Induced Lattice Oxygen Oxidation in Spinel Oxide for Superior Oxygen Evolution Reaction. *Angew. Chem. Int. Ed.* **2024**, e202416757.
- (12) Öyküm, N. A.; Luca, S.; Alessandro, F. Mechanisms of the Oxygen Evolution Reaction on  $\text{NiFe}_2\text{O}_4$  and  $\text{CoFe}_2\text{O}_4$  Inverse-Spinel Oxides. *ACS Catal.* **2022**, *12*, 9058–9073.
- (13) Imtiaz, A.; Biswas, Rathindranath, P. R. A.; Halder, K. K.; Singh, H.; Banerjee, B.; Kumar, B.; Ma, Y. R.; Haldar, K. K. Graphitic Carbon Nitride Composites with  $\text{MoO}_3$ -Decorated  $\text{Co}_3\text{O}_4$  Nanorods as Catalysts for Oxygen and Hydrogen Evolution. *ACS Appl. Nano Mater.* **2021**, *4*, 12672–12681.
- (14) Sivasankara Rao E.; Zhiping, L. Tuning the intrinsic catalytic activities of oxygen-evolution catalysts by doping: a comprehensive review. *J. Mater. Chem. A.* **2021**, *9*, 20131–20163.
- (15) Hengqi, L.; Rui, X.; Shengyu, M.; Ran, W.; Zhiguo, L.; Tai, Y.; Bo, S. Recent advances in noble-metal-free bifunctional oxygen electrode catalysts. *Energy Adv.* **2025**, *4*, 55-83.
- (16) Wei, X. Interactions between metal species and nitrogen-functionalized carbon nanotubes. *Catal. Sci. Technol.* **2016**, *6*, 630-644.
- (17) Wan, T. H.; Mattia, S.; Chi, C.; Francesco, C. Influence of the Discretization Methods on the Distribution of Relaxation Times Deconvolution: Implementing Radial Basis Functions with DRT tools. *Electrochim. Acta.* **2015**, *184*, 483-499.
- (18) Earl Matthew, D.; Arno, B.; Beatriz Roldan, C. Facet Dependence of the Oxygen Evolution Reaction on  $\text{Co}_3\text{O}_4$ ,  $\text{CoFe}_2\text{O}_4$ , and  $\text{Fe}_3\text{O}_4$  Epitaxial Film Electrocatalysts. *J. Am. Chem. Soc.* **2024**, *146*, 13770–13782.
- (19) Ghamarinia, M.; Babaei, A.; Zamani, C. Electrochemical characterization of  $\text{La}_2\text{NiO}_4$ -infiltrated  $\text{La}_{0.6}\text{Sr}_{0.4}\text{Co}_{0.2}\text{Fe}_{0.8}\text{O}_{3-\delta}$  by analysis of distribution of relaxation times. *Electrochim. Acta.*, **2020**, *353*, 136520.
- (20) Bharati, D.; Sahanaz, P.; Harsha, D.; Sayan, B. Oxygen-Defect-Rich Cobalt Ferrite Nanoparticles for Practical Water Electrolysis with High Activity and Durability. *ChemSusChem.* **2020**, *13*, 3875 – 3886.

- (21) Yue, Z.; Tao, L.; Yike, Y.; Weiji, D.; Yin'an, Z.; Ye, P. Stabilizing Oxygen Vacancy in Entropy-Engineered  $\text{CoFe}_2\text{O}_4$ -Type Catalysts for Co-prosperity of Efficiency and Stability in an Oxygen Evolution Reaction. *ACS Appl. Mater. Interfaces* **2020**, *12*, 32548–32555.
- (22) Jiang, Q.; Sihong, W.; Chaoran, Z.; Ziyang, S.; Haoyue, Z.; Ruohan, F.; Yuanman, N.; Xiaolan, T.; Yichuan, G.; Xinhong, Z.; Seunghwa, L.; Di, Z.; Fang, S. Active oxygen species mediate the iron-promoting electrocatalysis of oxygen evolution reaction on metal oxyhydroxides. *Nat Commun.* **2023**, *14*, 6826.
- (23) Biao, Z.; Yanan, W.; Keru, C.; Yuheng, Z.; Yuxiao, X.; Chunxia, L.; Qi, W. Cobalt Nanoparticles Embedded in N-Doped Porous Carbon for Efficient Alkaline Water Electrolysis. *Energy Fuels* **2023**, *37*, 15637–15646.
- (24) Juntong, S.; Jiayang, J.; Yatao, C.; Jing, W.; Qindong, Z.; Junjie, G. Unravelling Temperature Ramping Rates in Fabricating NaCl-Induced Porous Co/N-C Electrocatalysts for Oxygen Reduction Reaction. *ChemElectroChem* **2022**, *9*, e202200375.
- (25) Xiang, W.; Xu, H.; Du, R.; Congcong, X.; Xueqiang, Q.; Zhifu, L.; Pablo, G.; Jordi, A.; Andreu, C. Junshan, L. Cobalt Molybdenum Nitride-Based Nanosheets for Seawater Splitting. *ACS Appl. Mater. Interfaces* **2022**, *14*, 41924–41933.
- (26) Abinaya, N.; Charles Robert, M.; Srinivasan, N.; Saravanakumar, S.; Electron density mapping and bonding in Mn doped  $\text{CoFe}_2\text{O}_4$  using XRD, and its correlation with room temperature optical and magnetic properties. *J. Magn. Magn. Mater.* **2023**, *580*, 170938.